applied sciences

MDPI

Article

Analysis of Mixed-Mode I/II/III Fracture Toughness Based on a Three-Point Bending Sandstone Specimen with an Inclined Crack

Xin Pan [1], Jiuzhou Huang [1], Zhiqiang Gan [1], Shiming Dong [1,2,*] and Wen Hua [1,2,*]

[1] Key Laboratory of Deep Underground Science and Engineering, Ministry of Education, College of Architecture and Environment, Sichuan University, Chengdu 610065, China; pan-px@foxmai.com (X.P.); huangjiuz@126.com (J.H.); ganzhiqiang@stu.scu.edu.cn (Z.G.)

[2] Failure Mechanics and Engineering Disaster Prevention and Mitigation Key Laboratory of Sichuan Province, Sichuan University, Chengdu 615065, China

* Correspondence: smdong@scu.edu.cn (S.D.); wenhua@scu.edu.cn (W.H.)

Abstract: The crack-propagation form may appear as an arbitrary mixed-mode fracture in an engineering structure due to an irregular internal crack. It is of great significance to research the mixed-mode fracture of materials with cracks. The coupling effect of multiple variables (crack height ratio, horizontal deflection angle and vertical deflection angle) on fracture parameters such as the stress intensity factors and the T-stress are the key points in this paper. A three-point bending specimen with an inclined crack was proposed and used to conduct mixed-mode fracture research. The fracture parameters were obtained by finite element analysis, and the computed results showed that the pure mode I fracture and mixed-mode fractures (mode I/II, mode I/III and mode I/II/III) can be realized by changing the deflection angles of the crack. The pure mode I and the mixed-mode fracture toughness of sandstone were obtained by a series of mixed-mode fracture experiments. The experimental results were analyzed with the generalized maximum tangential strain energy density factor criterion considering T-stress. The results showed that the non-singular term T-stress in the fracture parameters cannot be ignored in any mixed-mode fracture research, and the generalized maximum tangential strain energy density factor criterion considering T-stress can better predict the mixed-mode fracture toughness than other criteria.

Keywords: mixed-mode I/II/III; three-point bending specimen with an inclined crack; sandstone; numerical and experimental study; generalized maximum tangential strain energy density factor criterion

check for updates

Citation: Pan, X.; Huang, J.; Gan, Z.; Dong, S.; Hua, W. Analysis of Mixed-Mode I/II/III Fracture Toughness Based on a Three-Point Bending Sandstone Specimen with an Inclined Crack. *Appl. Sci.* **2021**, *11*, 1652. https://doi.org/10.3390/app11041652

Academic Editors: Ricardo Branco and Giuseppe Lacidogna

Received: 19 December 2020
Accepted: 9 February 2021
Published: 12 February 2021

Publisher's Note: MDPI stays neutral with regard to jurisdictional claims in published maps and institutional affiliations.

Copyright: © 2021 by the authors. Licensee MDPI, Basel, Switzerland. This article is an open access article distributed under the terms and conditions of the Creative Commons Attribution (CC BY) license (https://creativecommons.org/licenses/by/4.0/).

1. Introduction

The pure mode I fracture is a common in-plane open fracture, and the mode I critical stress intensity factor (K_{IC}) is one of the important material properties characterizing material fractures. Extensive experimental research on the mode I fracture of metals [1], ceramics [2], PMMA [3,4] and rock [5–7] has been achieved by using different specimen configurations. However, it is necessary to consider mixed-mode fractures, owing to the disordered internal microcracks and the complex stress conditions in practical engineering materials and structures. A great deal of research has been done on mixed-mode fracture specimens related to mixed-mode I/II and I/III fractures. For example, the fracture loads of HMA from pure mode I to pure mode II by different loading methods were obtained at a low temperature [8]. The mixed-mode I/II fracture test of concrete showed that the fiber content has an effect on the fracture toughness [9]. The stress intensity factors (SIFs) and non-singular term (T-stress) were calculated, and the results showed that T-stress increased with the increase of crack angles in two disc-type specimens [10]. When the crack width was larger, the crack became a notch, and investigations of mixed-mode I/II fractures based on a U-notch [11] and a V-notch [12] were carried out. Theorical

and numerical simulation investigations of the SIFs of pure mode I, pure mode II and mixed-mode I/II have been carried out based on central crack disk specimens [13–15]. The mixed-mode I/II fracture experiments of central crack disk specimens were studied by using sandstone [16–18], limestone [19] and cement mortar [20]. A penalty-based cohesive element technology was presented [21,22] and used to develop an application for predicting delamination crack growth in mixed-mode I/II [23]. Even though the mixed-mode I/II fracture experiments of four-point bending were studied [24,25], the three-point bending specimen was more widely used, and the experimental parameters were easier to control. For example, the numerical simulation and experimental study of an edge-cracked semi-circular bend (SCB) specimen subjected to three-point bend loading have been carried out [26]. The effects of thickness and Poisson's ratio on 3D mixed-mode I/II fractures were studied by using edge-cracked semi-circular bend (SCB) specimens [27]. Further, mixed-mode I/II fracture experiments using SCB specimens with different materials, such as hot-mix asphalt (HMA) [8], marble [28], limestone [19], sandstone [29] and acrylonitrile butadiene styrene [30], have been tested and analyzed. The results showed that SCB specimens were suitable to study the fracture of HMA at a low temperature [8]. In addition to temperature, atmospheric pressure also should be considered when analyzing and predicting fractures [28]. The prediction of the crack initiation angle was affected by SIFs and the non-singular term (T-stress), and the value and sign of T-stress in the mixed-mode I/II fracture of SCB specimens played important roles [19]. The internal structure of the material also affected the fracture toughness and fracture mode [30]. An edge-cracked triangular (ECT) specimen and an edge-cracked short-bend beam specimen of mixed-mode I/II fracture were also studied [31,32]. In addition, the effect of crack angles on mixed-mode I/III fractures has also been studied. Mode I SIF increased for the angle between crack and loading direction, but mode III SIF decreased [33]. Mixed-mode I/III fatigue-fracture studies have also been carried out, and the results showed that increasing the crack angle and decreasing the crack length can effectively increase the fatigue life [34]. It was found that the prediction of crack initiation can be enhanced by considering the plastic zone and friction on the crack surface of I/III mixed-mode fractures [35]. The edge-notched disc bend (ENBD) specimen has been proposed to be suitable for mixed-mode I/III fractures, and can realize a pure mode III fracture [36]. Mixed-mode I/III fracture experiments have been carried out on various materials such as marble [37,38], asphalt concrete [38,39], PMMA [38] and graphite [38,40] by using ENBD specimens, and the mode III fracture toughness was less than the mode I fracture toughness for each material. It was found that the crack surface broke suddenly in mixed-mode I/III fractures by using a three-point bending specimen with a large thickness and an inclination angle less than 10°, and a relationship between the scale of the fragmentation and the mixed mode was established [41]. In another investigation of mixed-mode I/III fractures, the crack deflection angles of the specimen achieved larger inclination angles, but only four groups of inclination angles were considered, and the crack depth was fixed and low [42], so the persuasiveness of the research results was inadequate.

In order to study the initiation and propagation of cracks, some fracture criteria, such as the maximum tangential stress (MTS) criterion [43], the maximum tangential strain (MTSN) criterion [44] and the maximum tangential strain energy density (MTSED) criterion [45] were proposed and frequently used to analyze the fracture characteristics. These criteria only considered the singular term of the stress field at the crack tip and ignored the non-singular term (T-stress). However, a large number of experiments have proven that the fracture criterion considering the non-singular term can predict the experimental results more effectively [16–20,26,28,30,31,37–40]. It was found that the generalized maximum tangential stress (GMTS) or generalized maximum tangential strain (GMTSN) criteria, both considering T-stress, can better predict the central cracked disc experimental results of mixed-mode I/II fractures compared with the MTS criterion [16–20]. The GMTS criterion was also used to predict and verify the experimental results of three-point bending specimens in mixed-mode I/II fracture studies, whether SCB or ETC speci-

mens [26,28,30,31]. The mixed-mode I/III fracture experimental results for various materials such as marble [37], asphalt concrete [39] and graphite [40] using ENBD specimens were in good agreement with the theoretical predicted value of the MTSED criterion without considering T-stress. The experimental results of pure mode III fracture toughness were also in good agreement with the theoretical predictions of the MTSED criterion [38]. However, an extended MTSED criterion considering T-stress was proposed, which was considered to better predict the testing results of ENDB specimens, especially for the pure mode III case [46].

Most of the existing studies on mixed-mode fractures involve I/II and I/III fractures. The mixed-mode I/II/III fracture is rare, and the applicability of the existing criteria to mixed-mode I/II/III fractures still needs more study. Therefore, based on the previous investigations, a mixed-mode fracture test configuration, called the three-point bending specimen with inclined crack (TPB-IC), was proposed in this study. By changing the deflection angles of the crack in two directions, it can cover most ranges of mode I/II/III mixed fractures. The influences of the deflection angles and crack length on fracture parameters (i.e., SIFs and T-stress) and the experiments of the TPB-IC specimen made of sandstone for mixed-mode I/II/III fracture were carried out. Through the extended analysis of the MTSED criterion, the generalized maximum tangential strain energy density (GMTSED) criterion considering T-stress was obtained, and a unified and complete three-dimensional expression under the conditions of plane stress and plane strain was derived. The experimental results and the predicted values of the GMTSED criterion considering the three-dimensional T-stress were comparatively analyzed.

2. The TPB-IC Specimen for Mixed-Mode I/II/III Fracture Study

2.1. The TPB-IC Specimen for the Mixed-Mode I/II/III Fracture Model

The loading configuration and geometric structure of the TPB-IC specimen for a mixed-mode I/II/III fracture are shown in Figure 1. The TPB-IC specimen is a rectangular beam of length (L), thickness (B) and height (W). It contains a straight edge crack of length (a) in the direction of the through thickness. a/W is defined as the crack height ratio of the specimen. The specimen is supported in a three-point bending fixture with a span (S). On the top of the specimen, there is a uniformly distributed load (P) applied along the thickness direction. The crack forms an angle α with the loading line on the bottom surface of the specimen, which is defined as the horizontal deflection angle (Figure 1c). The crack on the front surface of the specimen forms an angle β with the vertical direction, which is defined as the vertical deflection angle (Figure 1b). When α and β are both zero, the loading conditions and the geometry are symmetrical, and the specimen fails through a pure mode I fracture. However, for other angles α and β, the loading conditions and the geometry are asymmetric with respect to the crack surface, and mixed-mode fracture occurs in the specimen. The crack deflection angles α and β are the principal influencing parameters in mixed-mode fracture. The contribution of mode I, mode II and mode III SIFs in mixed fractures depends on α and β.

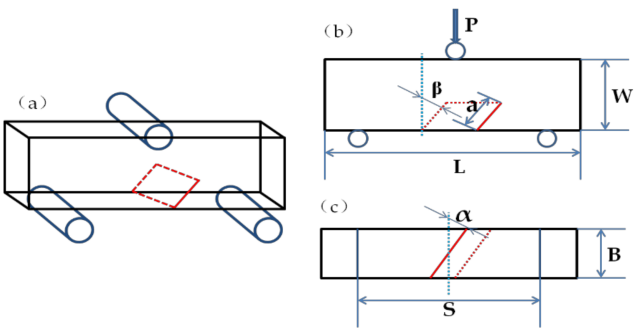


Figure 1. The loading configuration and geometry of the TPB-IC specimen. (**a**) Panorama of specimen loading. (**b**) Front view of specimen loading. (**c**) Bottom view of specimen loading.

2.2. Numerical Simulation of the TPB-IC Specimen

In this study, the mixed-mode fracture parameters of the TPB-IC specimens were determined accurately based on the ABAQUS software and J-integral method. The finite element analysis defined a series of element groups around the crack tip for generating different closed paths when solving the SIFs and T-stresses. Due to the singularity of the stress-strain field at the crack tip, it was necessary to consider the singular elements at the crack tip, which can be achieved by moving the middle node of the element of the first integral loop around the crack tip to a quarter distance near the crack front [27]. The full field solution of the stress at the crack tip was obtained through finite element analysis.

The three-dimensional finite element models of the TPB-IC specimen with various crack height ratios and crack deflection angles were established and analyzed. According to previous fracture studies [36], the parameters of the crack tip of the specimen models were functions of the specimen geometry (B and W), support span (S), crack length (a), load (P) and crack deflection angles (α and β). The expressions of the fracture parameters were as follows:

$$K_I = \frac{PS}{BW^{3/2}} Y_I(a/W, \alpha, \beta) \quad (1)$$

$$K_{II} = \frac{PS}{BW^{3/2}} Y_{II}(a/W, \alpha, \beta) \quad (2)$$

$$K_{III} = \frac{PS}{BW^{3/2}} Y_{III}(a/W, \alpha, \beta) \quad (3)$$

$$T = \frac{PS}{BW^2} T^*(a/W, \alpha, \beta) \quad (4)$$

where Y_I, Y_{II} and Y_{III} and T* are the dimensionless SIFs and T-stresses, which are functions of the crack height ratio a/W, horizontal deflection angle α and vertical deflection angle β, respectively. In order to ensure the accuracy of the simulation results, the crack tip region was densified and optimized, and different element sizes of the same models were compared. The results showed that different element sizes had little effect on the results, and the error was less than 1%, as seen in Table 1. The origin of the values in Table 1 will be explained later. Considering comprehensively, 2 mm was determined as the element size for this simulation. The finite element analysis of the specimen models consisted of more than 95,000 solid elements (c3d15 elements at the crack tip, c3d20 elements in the surrounding area near the crack and c3d10 elements far away from the crack), allowing construction of a three-dimensional fracture model with different crack height ratios, and different horizontal and vertical deflection angles. Figure 2 shows a three-dimensional grid pattern of the specimen and a zoomed view of the crack tip region. The material of model is assumed to be linear elastic and isotropic. The material characteristics and geometric dimensions of the TPB-IC specimen for finite element analysis are shown in Table 2.

Table 1. Dimensionless T-stresses and SIFs for the finite element model of the TPB-IC specimen of different element sizes when a/W = 0.5, $\alpha = 30^\circ$ and $\beta = 30^\circ$.

Element Sizes	T*	Y_I	Y_{II}	Y_{III}	Computation Time
1 mm	3.5864	1.2778	0.4694	0.5165	2967 s
2 mm	3.5736	1.2767	0.4698	0.5172	66 s
3 mm	3.5712	1.2745	0.4687	0.5186	19 s
4 mm	3.5926	1.2722	0.4691	0.5194	7 s

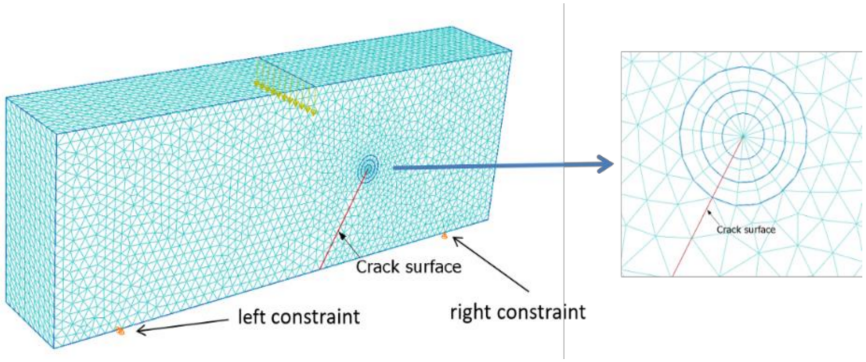


Figure 2. Finite element model and zoomed view of crack tip region for the TPB-IC specimen.

Table 2. Material characteristics and geometric dimensions given for the finite element model of the TPB-IC specimen.

Parameter	Numerical Value
S	90 mm
B	20 mm
W	40 mm
a	From 4 to 28 mm
E	5 GPa
P	100 N
ν	0.35
α	From 0° to 60°
β	From 0° to 60°

The fixed displacement constraints were set at the bottom of the TPB-IC specimen. As shown in Figure 2, the constraint of horizontal and vertical directions on the left side was 45 mm from the center of the bottom, and the constraint of vertical direction on the right side was 45 mm from the bottom center, so as to achieve static constraint of the TPB-IC specimen. The distances between two sections of displacement constraint and the center of the TPB-IC specimen were equal, and the constraint distance (i.e., span S) was fixed at 90 mm. The crack was a natural crack without any constraints. All finite element analysis results for the SIF and T-stress on different crack height ratios, horizontal deflection angles and vertical deflection angles were obtained.

In the finite element model, the standardized parameter of the crack tip along the thickness direction was defined as z/B. This means that z/B = 0 refers to the middle position of the crack, and z/B = ±1 refers to the free surface of the TPB-IC specimen. The mode I SIF at the middle section of the thickness, i.e., z/B = 0, was defined as K_{Im}, and the T-stress in the middle section was defined as T_m. The effective SIF was defined as:

$$K_{eff} = \sqrt{K_I^2 + K_{II}^2 + K_{III}^2} \quad (5)$$

By using the finite element analysis results of the crack tip along the thickness divided by K_{Im} and T_m respectively, the normalized SIFs and T-stress can be obtained. Figure 3 shows the normalized results of four groups of crack deflection angles (α = 0°, β = 0°, α = 0°, β = 30°, α = 30°, β = 0° and α = 30°, β = 30°) under the conditions of crack height ratio a/W = 0.5 and span S = 90 mm. According to Figure 3, the three-dimensional effect on the SIFs and T-stress can be observed at different positions of the crack tip. When α = 0°, β = 0° (Figure 3a), K_{II} and K_{III} were always zero, so the pure mode I fracture can be well realized. In the middle part of the crack, i.e., −0.6 < z/B < 0.6, there was almost no change in K_I. There was a deviation (about 20%) near the free surface (z = ± 1). The investigations of SIFs in a three-dimensional specimen proved the SIF of the free surface decreased relative to the middle interface [36,38]. For other angles (see Figure

3b–d), all SIFs, including the effective SIF K_{eff}, had a sudden change near the free surface, but the portion near the middle of the crack tended to be stable. When $\alpha = 0°$ and $\beta = 30°$, K_{III} tended to be 0 in the middle position, and the specimen was subjected to a mixed-mode I/II fracture. When $\alpha = 30°$, $\beta = 0°$, K_{II} tended to be 0 in the middle position, so the specimen was mainly subjected to a mixed-mode I/III fracture. When $\alpha = 30°$, $\beta = 30°$, the specimen was subjected to a mixed-mode I/II/III fracture. It is worth noting that the negative value here only represents the direction. In order to visualize the size relationship of the SIFs, the absolute values of the SIFs are used directly in later sections.

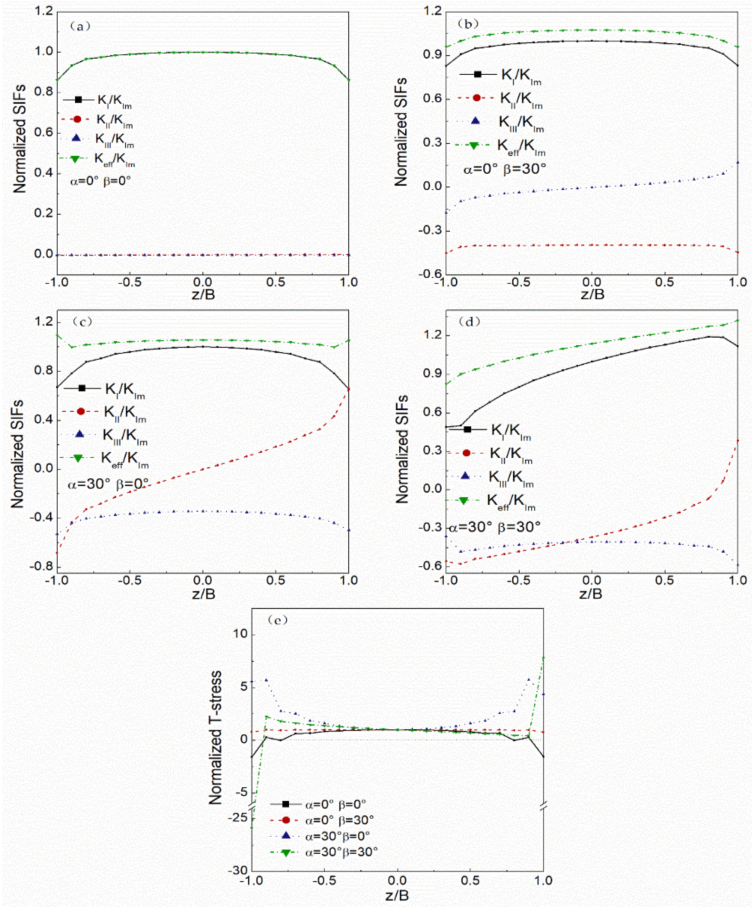


Figure 3. Variations of the normalized fracture parameters for typical crack inclined angles (α and β) along z/B direction. (**a**) The normalized SIFs in $\alpha = 0°$ and $\beta = 0°$. (**b**) The normalized SIFs in $\alpha = 0°$ and $\beta = 30°$. (**c**) The normalized SIFs in $\alpha = 30°$ and $\beta = 0°$. (**d**) The normalized SIFs in $\alpha = 30°$ and $\beta = 30°$. (**e**) The normalized T-stress in four groups of angles.

In the four groups of crack deflection angles, the crack tip normalized T-stresses are shown in Figure 3e when $-1 \leq z/B \leq 1$. The variation of the normalized T-stress was similar to the SIFs along the thickness direction. There was almost no change in the middle position, but the deviation of normalized T-stress at the free surface was more obvious than the SIFs for different horizontal and vertical deflection angles. For example, when $\alpha = 30°$, $\beta = 30°$, there was a difference of more than 25 times between the T-stress of $z/B = \pm 1$ at the free surface and the middle of the model.

Even though the deviation between the free surface and the middle position was large, according to the research of Bazant and Estensoro [47], the singularity of the stress field near the free surface or corner is different from the traditional definition of the stress-strain field at the crack tip. Thus, the simulation results near the free surface of the specimen can be ignored. In the study of the effects of thickness and Poisson's ratio by Aliha and Saghafi [30], the SIFs and T-stress in the middle position of the crack were taken as the

simulation result, and a good research achievement was seen. Our study also used that method. The SIFs and T-stresses in the middle of the crack (z/B = 0) were taken as the finite element simulation result of the TPB-IC specimen.

It was necessary to verify the correctness of the simulation results. The existing SIF formulas in the relevant literature were used to compare with the numerical results in this study. The usual formula for the dimensionless SIF of mode I fracture of three-point bending specimen is [7]:

$$Y_{If} = 2.9\left(\frac{a}{W}\right)^{1/2} - 4.6\left(\frac{a}{W}\right)^{\frac{3}{2}} + 21.8\left(\frac{a}{W}\right)^{\frac{5}{2}} - 37.6\left(\frac{a}{W}\right)^{\frac{7}{2}} + 38.7\left(\frac{a}{W}\right)^{9/2} \quad (6)$$

Taking the results of a/W of 0.1, 0.3, 0.5 and 0.7 for comparison, the data in Table 3 were obtained. From Table 3, it is shown that the relative error of the calculation value and the formula was within 5%, and the relative error was 1.25% which is minimal with a/W = 0.5. At the same time, according to the experimental data of Jianping Zuo [7], the fracture load and specimen parameters of 25 °C at room temperature were used in the numerical modeling of this study. The corresponding K_I value was obtained from the numerical solution seen Table 4. It is shown in Tables 3 and 4 that the numerical results obtained in this study had satisfactory accuracy and effectiveness. The verification of Y_{II} and Y_{III} can also be obtained by the same method.

Table 3. Comparison between formula values and the numerical results of the dimensionless mode I SIF.

a/W	Y_{If}	Y_I	Relative Error
0.1	0.8299	0.8090	2.52%
0.3	1.5228	1.4887	2.24%
0.5	2.6649	2.6316	1.25%
0.7	5.6534	5.9142	4.61%

Table 4. Comparison of experimental and calculated values of mode I fracture toughness.

W (mm)	B (mm)	a (mm)	P (N)	K_{IC} Experimental Data [7] (Mpam$^{1/2}$)	K_{IC} Numerical Results (Mpam$^{1/2}$)
10.03	5.15	4.99	95.6	0.9771	0.9903

The fracture parameters K_I, K_{II}, K_{III} and T of the specimen were found by numerical simulation, and can be transformed into dimensionless expressions (Y_I, Y_{II}, Y_{III} and T*) by Equations (1)–(4), respectively. Figure 4 shows the variation of Y_I, Y_{II} and Y_{III} under different crack height ratios for a/W = 0.1–0.7 and four groups of typical horizontal and vertical deflection angles. It can be seen from Figure 4 that all the ranges of the crack height ratio did not change the mixed-mode fracture. The crack height ratio a/W had the same effect on the variations of the dimensionless SIFs. The value of Y_I, Y_{II} and Y_{III} increased with the increase of crack height ratio, and the change rate of Y_I clearly increased with high crack height ratio. When the vertical deflection angle $\beta = 0°$, no matter what the values of the crack height ratio a/W and the horizontal deflection angles α were, Y_{II} was almost constant at zero. In this case, the specimen was subjected to a mixed-mode I/III fracture. When the horizontal deflection angle $\alpha = 0°$, similarly, Y_{III} was almost constant at zero, and the specimen suffered a mixed-mode I/II fracture. This phenomenon is consistent with the investigation of the mixed-mode fracture of Aliha's edge-notched disc and semicircle disk [26,30,36–38].

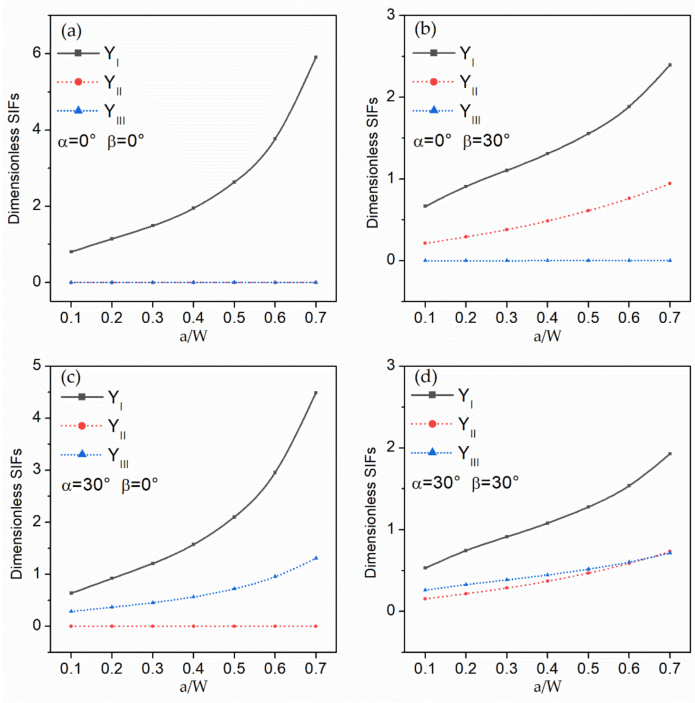


Figure 4. The relationship between dimensionless SIFs and crack height ratio a/W for typical crack inclined angles. (**a**) The normalized SIFs in $\alpha = 0°$ and $\beta = 0°$. (**b**) The normalized SIFs in $\alpha = 0°$ and $\beta = 30°$. (**c**) The normalized SIFs in $\alpha = 30°$ and $\beta = 0°$. (**d**) The normalized SIFs in $\alpha = 30°$ and $\beta = 30°$.

In order to further research the relationship between the dimensionless SIF and crack deflection angles α and β, models with span S = 90 mm and crack height ratio a/W = 0.5 were selected. All the simulation results are shown in Figure 5. The effect of the crack deflection angles on one of the fracture parameters is shown by two graphs in each row of Figure 5. For example, according to Figure 5a,b, by increasing α and β, Y_I decreased but the decrease amplitudes were not the same. The decrease rate of Y_I increased with the increase of α, but it tended to be mild with the increase of β. Each column graph (Figure 5a,c,e) in Figure 5 shows the effect of one crack deflection angle on the three fracture parameters. By increasing horizontal deflection angle α, the value of Y_I and Y_{II} became less, but the magnitude value of Y_{III} increased first and then decreased. The maximum value of Y_{III} was obtained when $\alpha = 45°$. In general, the independent change of the crack deflection angle did not affect the effect of the other angles on the dimensionless parameters, but did affect the value size shown in Figure 5.

Therefore, the analysis of the simulation results indicated that when the span was fixed and the crack height ratio a/W and β increased, a pure mode II fracture of the TPB-IC specimen could be obtained. If the span was changed, a/W and β of the pure mode II fracture were correspondingly changed. For example, Mousavi [32] used short specimens with short spans to achieve a pure mode II fracture. Table 5 also shows the corresponding span S, angle value of β and crack height ratio a/W of the pure mode II fracture, or close to pure mode II fracture. According to the previous result, if the specimen suffers a pure mode III fracture, K_{II} needs to be kept at zero and the value of α changes only under the condition of $\beta = 0°$. However, no matter what the values of the crack height ratio a/W and α were, K_I was not zero, as seen in Figure 5a. Thus, pure mode III fractures and mixed-mode II/III fractures cannot be realized using this specimen, which is similar to the investigations of Lin [41] and Ahmadi-Moghadam [42].

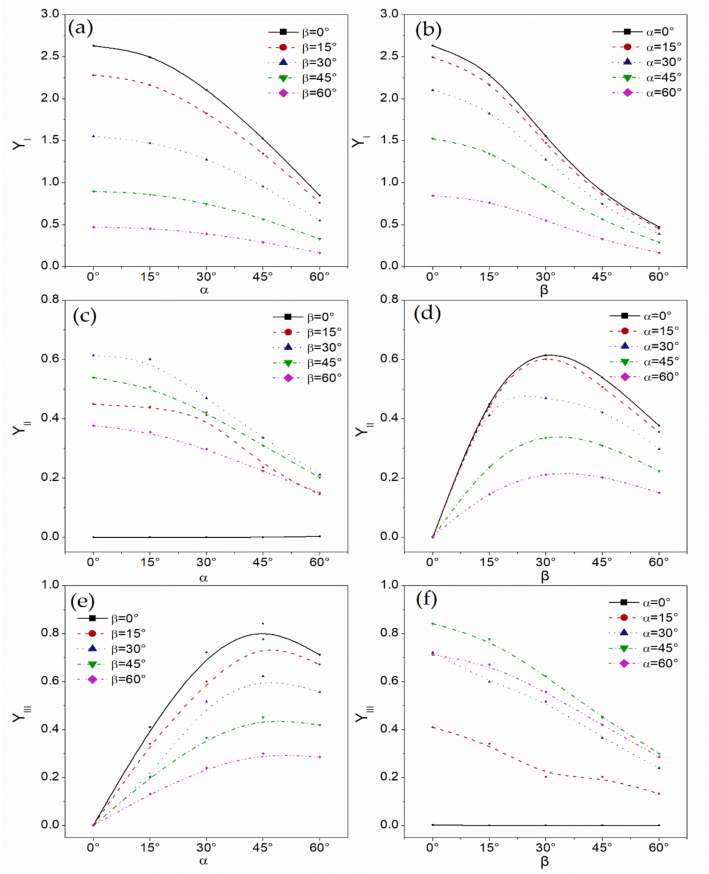


Figure 5. The relationship between dimensionless SIFs Y_I, Y_{II} and Y_{III} with respect to horizontal deflection angle α and vertical deflection angle β. (**a**) The relationship between Y_I and α. (**b**) The relationship between Y_I and β. (**c**) The relationship between Y_{II} and α. (**d**) The relationship between Y_{II} and β. (**e**) The relationship between Y_{III} and α. (**f**) The relationship between Y_{III} and β.

Table 5. Pure mode II fracture angle values corresponding to different span S and a/W.

S (mm)	a/W	β (°)	$K_I\left(\mathbf{MPa}^{1/2}\right)$	$K_{II}\left(\mathbf{MPam}^{1/2}\right)$	$K_{III}\left(\mathbf{MPam}^{1/2}\right)$
90	0.9	68	0.00	0.18	0.00
60	0.7	50	−0.03	0.53	0.00
48	0.5	49	0.01	0.50	0.00

Figure 6 shows the variation of the dimensionless T-stress (i.e., T*) for different crack height ratios a/W. According to Figure 6, no matter what mixed-mode fracture is considered, T* increased with an increasing crack length. Furthermore, when the vertical deflection angle β was small, T* had a negative value for the two curves of β = 0° in the case of low crack height ratio. Figure 7 shows the variations between the crack deflection angles and T*, but the variations are relatively complex. As shown in Figure 7a, when β was large, by increasing α, T* decreased. When β was small, the change of T* cannot be clearly determined due to its relatively small value and small change. From the observation in Figure 7b, except for α = 60°, T* increased with an increasing β, and the peak value was obtained when β = 45°.

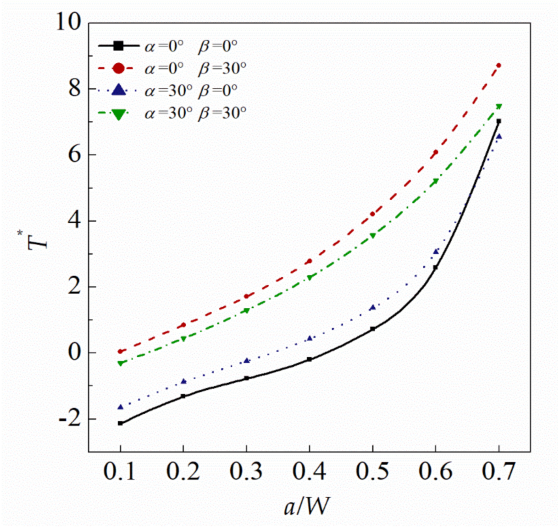


Figure 6. Variation of dimensionless T-stress T* under typical crack inclined angles for varying values of crack height ratio *a*/*W*.

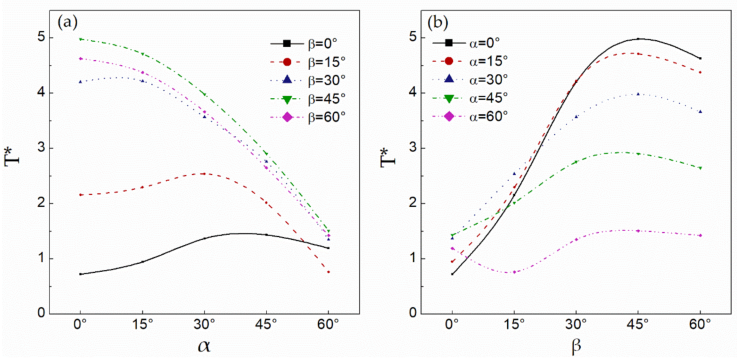


Figure 7. Variation of dimensionless T-stress T* with respect to horizontal deflection angle α and vertical deflection angle β. (**a**) The relationship between T* and α. (**b**) The relationship between T* and β.

The relationship between the nonsingular term T relative and the singular term SIFs in the mixed-fracture process was considered and usually defined by biaxiality ratio B [10], which is defined as:

$$B = \frac{T\sqrt{\pi a}}{K_{eff}} \tag{7}$$

The larger the parameter B of the fracture specimen was, the more important the T-stress was in the mixed-fracture behavior. Figure 8 shows the variations under different vertical and horizontal deflection angles. It can be seen from Figure 5b that the biaxiality ratio B had a significant change, in the range of 0~2.5. So, the influence and importance of T-stress on the mixed fracture of specimens is obvious.

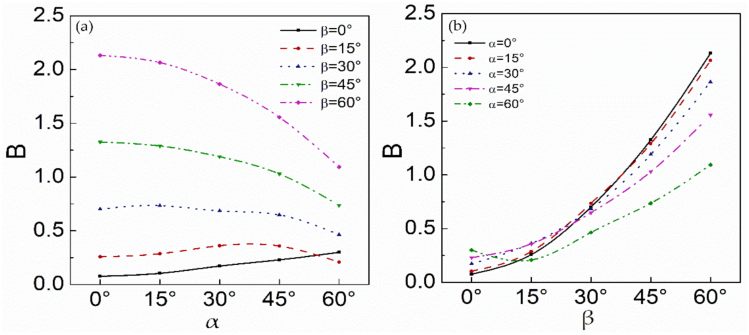


Figure 8. Variation of biaxiality ratio B with respect to horizontal deflection angle α and vertical deflection angle β. (**a**) The relationship between B and α. (**b**) The relationship between B and β.

The three-dimensional mixed-mode fracture experiments using TPB-IC specimens were carried out with typical sandstone materials, and the influence of fracture parameters on mixed-mode fractures is analyzed in the next sections.

2.3. Experimental Investigation of TPB-IC Specimens

Sandstone was selected as the material for the 3D mixed-mode fracture experiments using the TPB-IC specimen because of its low price, convenient processing, wide distribution and application in various engineering projects and experimental research. All the specimens in this experiment were taken from one large homogeneous piece of sandstone. The stone was cut into 20 mm thin sections, and then the thin sections were cut into long rectangular specimens of sizes (120 mm long and 40 mm wide). The cracks with different horizontal and vertical rotation angles were cut out using a circular slicer with a thickness of only 0.8 mm. The crack tip was sawn again with a 0.3 mm thick saw line, which made the crack height ratio a/W reach 0.5. The specimens were tested four times for each angle, and the experiments were carried out on the same universal compression testing machine (Figure 9). This consistent manufacturing and experimental process eliminated part of the error sources.

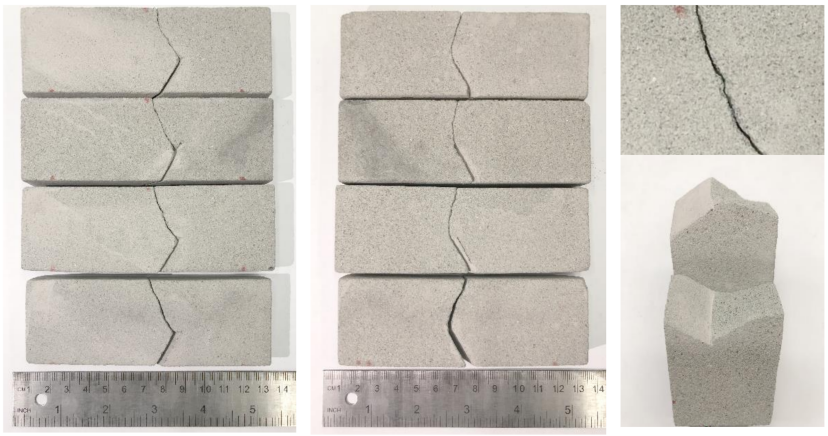


(**a**) (**b**)

Figure 9. (**a**) The full view of experimental machine. (**b**) The loading situation.

The specimens were loaded at a constant rate of 0.05 mm per minute until a fracture occurred. The fractured TPB-IC specimens (α = 30° β = 30°) are shown in Figure 10. When the loading began, the crack tip was under tensile effect and the upper and lower crack surfaces opened, which resulted in a mode I deformation. Due to the existence of a horizontal deflection angle, the deformation direction of the front-to-back crack was opposite, and the crack surface rotated and resulted in a mode III deformation. The relative displacement of the upper and lower crack surfaces occurred because of the vertical deflection angle, so the crack surfaces sheared, and the mode II deformation occurred. The crack propagation of the specimens started from the crack tip and then propagated

to the loading site (Figure 10a,b). Although the end of the crack propagation path was far away from the loading point and stopped at a small displacement from the loading point (see Figure 10a), it was believed that when the specimen height was large enough, the final end of the crack propagation path would reach the loading point, as in previous experimental results for large thickness on I/III mixed-mode fractures [48]. The kinks and deflections of the crack propagation path appeared during the I/II/III mixed-mode fracture seen Figure 10c. Although kinks were common in composite fractures [49], the same phenomenon occurred in a fracture experiment using sandstone when the displacement gradient of the crack propagation of sandstone was large, which led a displacement discontinuity of the crack surface [50]. Figure 10c shows the obvious deflection of the crack during crack propagation, which indicates that K_{II} and K_{III} have a significant influence on the mixed-mode fracture behavior.



(**a**) (**b**) (**c**)

Figure 10. The fractured TPB-IC specimen when $\alpha = 30^\circ$ and $\beta = 30^\circ$. (**a**) The front of the fractured specimens. (**b**) The back of the fractured specimens. (**c**) A close view of fracture surface.

Nine groups of load-displacement curves are shown in Figure 11. The load-displacement curves are concave curves with low loads and are short. This is because there were some microparticles on the surface of sandstone and microcracks in the interior, and the specimen was not compacted at the beginning of loading. However, it can be seen from the subsequent curve that there was a linear relationship between the displacement and load before the peak load. So, sandstone can be assumed to be a linear elastic material. The same phenomenon was found in the investigation on the correlation of mode II fracture toughness of sandstone with tensile strength [51]. In the case of three-point bending, the inclined crack needed more fracture load and fracture energy than the straight crack, which made the fracture load of the inclined crack specimen increase [32]. This is why the displacement and fracture were the largest when $\alpha = 60^\circ$ and $\beta = 60^\circ$. The peak fracture load curves at different angles are shown in Figure 12. When the horizontal deflection angle α increased, the fracture load increased in a small range globally, and the maximum change was less than 1.46 times (for the vertical deflection angle $\beta = 30^\circ$). However, with the increase of vertical deflection angle β, the fracture load increased gradually, and the maximum change was more than 3.13 times at $\alpha = 15^\circ$. Although certain errors were considered and reduced in the experiments, the deviation of each group of experimental fracture loads still occurred. This may be due to the distribution of internal microcracks and microdefects, or manual machining and grinding the crack tip by using blades. By substituting the critical peak load obtained from the experiment into Equations (1)–(4), where the corresponding geometric factors Y_I, Y_{II} and Y_{III} are extracted from the above diagram (Figure 5), and referring to Table 6, the fracture toughness of different mixed-mode fractures can be obtained. The experimental results, including the fracture load and corresponding fracture

toughness, are shown in Tables A1 and A2. More details on the fracture toughness analysis are given in the next section.

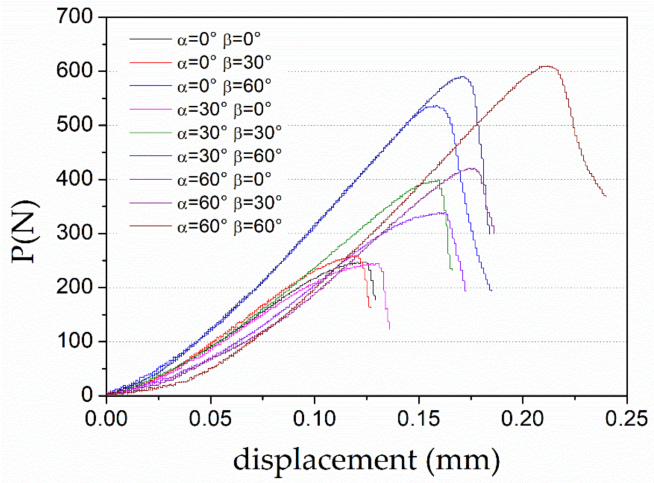


Figure 11. Curve of displacement and load with respect to horizontal vertical deflection angles.

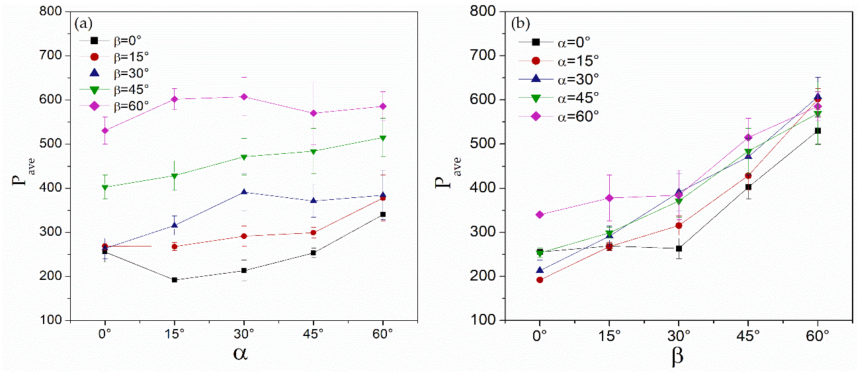


Figure 12. Variation of fracture load P_{ave} with respect to horizontal deflection angle α and vertical deflection angle β. (**a**) The relationship between P_{ave} and α. (**b**) The relationship between P_{ave} and β.

Table 6. Values of dimensionless SIFs at various horizontal and vertical deflection angles.

SIFs	Y_I					Y_{II}					Y_{III}				
β \ α	0°	15°	30°	45°	60°	0°	15°	30°	45°	60°	0°	15°	30°	45°	60°
0°	2.632	2.494	2.102	1.525	0.846	0.000	0.000	0.000	0.000	0.000	0.000	0.410	0.721	0.842	0.713
15°	2.282	2.163	1.824	1.346	0.761	0.449	0.440	0.412	0.237	0.145	0.000	0.341	0.600	0.776	0.671
30°	1.554	1.471	1.277	0.952	0.550	0.614	0.602	0.470	0.336	0.211	0.000	0.203	0.517	0.623	0.557
45°	0.897	0.860	0.747	0.566	0.330	0.540	0.508	0.421	0.310	0.202	0.000	0.203	0.366	0.451	0.419
60°	0.473	0.452	0.392	0.291	0.166	0.377	0.355	0.298	0.224	0.150	0.000	0.133	0.240	0.301	0.286

3. Fracture Toughness and Criterion Analysis

The pure mode I fracture toughness K_{IC} of the tested sandstone material was 0.38 MPa$\sqrt{m}$ according to the experimental results calculation. K_{IC} in the sandstone experiment conducted by Hua [52] was about 0.187 MPa$\sqrt{m}$, and that in the sandstone experiment conducted by Dehestani [53] was 0.6 MPa$\sqrt{m}$. The experimental value in this study was around midway between them. Considering the influence of regional factors and sandstone types, the value from the experiment was within the normal range of K_{IC} for sandstone. When the crack deflection angles α = β = 0°, the mixed-mode fracture toughness ratio $K_{II}/K_{IC} = K_{III}/K_{IC} = 0$. For other crack deflection angles, when α = 0° and β = 60°, K_I/K_{IC}

was about 0.387, and K_{II}/K_{IC} was about 0.307. When $\alpha = 60$, $\beta = 0$, K_I/K_{IC} was about 0.426, and K_{III}/K_{IC} was about 0.361. As mentioned above, the mixed-mode fracture toughness is also related to the presence of T-stress in the TPB-IC specimens. Therefore, when analyzing the fracture toughness of TPB-IC specimens, the traditional MTS criterion, MTSN criterion and MTSED criterion cannot be used for accurate predictions. However, it was shown that the generalized maximum tangential strain energy density (GMTSED) criterion can significantly improve the prediction of experimental results by considering the influence of T-stress, in addition to K_I, K_{II} and K_{III}.

Under the loading condition of general mixed-mode fractures, the elastic stress field at the crack tip can be expressed as a tensor S:

$$S = \begin{bmatrix} \sigma_r & \sigma_{r\theta} & \sigma_{rz} \\ \sigma_{\theta r} & \sigma_\theta & \sigma_{\theta z} \\ \sigma_{zr} & \sigma_{z\theta} & \sigma_z \end{bmatrix} \quad (8)$$

where σ_r, σ_θ, σ_z, $\sigma_{r\theta}$, $\sigma_{z\theta}$ and σ_{rz} are the stress components near the crack tip, which are available in literature [54], and r and θ are the coordinates of the crack tip, as illustrated in Figure 13.

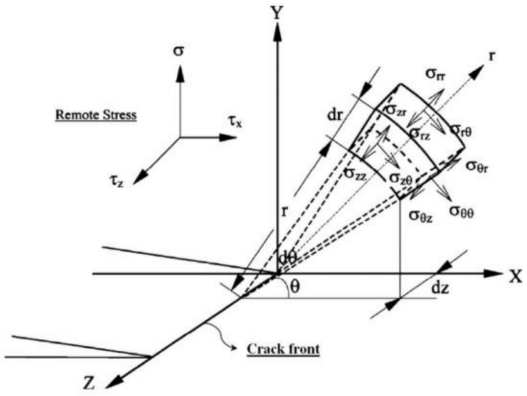


Figure 13. Mixed-mode I/II/III stress fields near the crack tip [46].

The stress state in the initial coordinate plane (θ–z) was assumed to be equal to the angle of rotation of element ϕ around the r-axis at the initial stage of crack propagation (Figure 14), so the stress tensor after coordinate transformation S′ is expressed as:

$$S' = QSQ^T = \begin{bmatrix} \sigma_r & \sigma_{r\theta'} & \sigma_{rz'} \\ \sigma_{\theta' r} & \sigma_{\theta'} & \sigma_{\theta' z'} \\ \sigma_{z' r} & \sigma_{z'\theta'} & \sigma_{z'} \end{bmatrix} \quad (9)$$

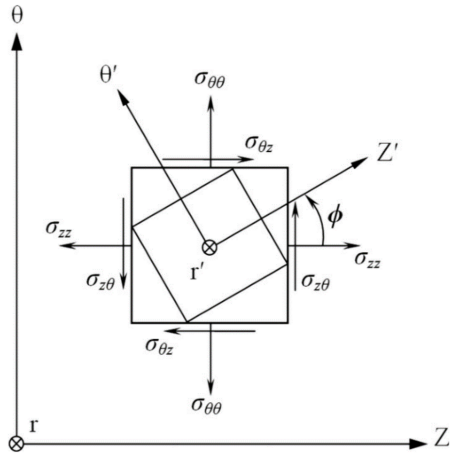


Figure 14. Stress state in the θ–z plane [46].

Q is the transformation matrix and is expressed as:

$$Q = \begin{bmatrix} 1 & 0 & 0 \\ 0 & cos\phi & -sin\phi \\ 0 & sin\phi & cos\phi \end{bmatrix} \quad (10)$$

The GMTSED criterion considering the combined effect of tangential stress and tangential strain in three-dimensional fracture parameter was used to predict the fracture test results of sandstone materials. Therefore, according to the definition of the GMTSED criterion, the tangential strain energy density factor can be calculated from:

$$C = \frac{1}{2} r \sigma_{\theta'} \varepsilon_{\theta'} \quad (11)$$

Due to the three-dimensional mixed-mode fracture, the plane strain state of σ_z was adopted. According to Hooke's law, $\varepsilon_{\theta'} = [\sigma_{\theta'} - v(\sigma_r + \sigma_{z'})]/E$, therefore the tangential strain energy density factor C is:

$$C = \frac{1}{4\pi E}\left\{m_{11}K_I^2 + m_{22}K_{II}^2 + m_{33}K_{III}^2 + m_{44}(B\eta K_{eff})^2 + m_{12}K_IK_{II} + m_{13}K_IK_{III} + m_{23}K_{II}K_{III} + (m_{14}K_I + m_{24}K_{II} + m_{34}K_{III})B\eta K_{eff}\right\} \quad (12)$$

where η is the relative critical distance defined as $\eta = \sqrt{\frac{2r}{a}}$. Ayatollahi and Saboori [45] and Hua [46] used α to represent the relative critical distance, however, α was used to represent horizontal deflection angle in the previous section, so η was used here. All the coefficients (m_{ij}) are shown in Tables A3 and A4.

According to the hypothesis of the GMTSED criterion, a mixed-mode fracture occurs when the maximum tangential strain energy density factor C reaches a maximum under the critical load near the crack tip. The angle and condition of crack propagation based on the GMTSED criterion are as follows:

$$\frac{\partial C}{\partial \theta} = 0, \frac{\partial C}{\partial \phi} = 0 \quad (13)$$

and sufficient conditions:

$$\frac{\partial^2 C}{\partial \theta^2}\left\langle 0, \frac{\partial^2 C}{\partial \theta^2}\frac{\partial^2 C}{\partial \phi^2} - \left[\frac{\partial}{\partial \phi}\left(\frac{\partial C}{\partial \theta}\right)\right]^2 \right\rangle 0 \quad (14)$$

The second hypothesis can also be written as:

$$C(\theta_0, \phi_0) = C_{cr} \quad (15)$$

where θ_0 and ϕ_0 are the in-plane and out-of-plane initiation angles, respectively, and are calculated from Equations (13)–(15). When a pure I mode fracture occurs, $K_{II} = K_{III} = 0$, $\theta_0 = \phi_0 = 0$, $K_I = K_{IC}$, C_{cr} is expressed using K_{IC} as:

$$C_{cr} = \begin{cases} \frac{1}{4\pi E}[1-(2v+1)v-2vB_I\eta]K_{IC}^2 & (plane\ strain) \\ \frac{1}{4\pi E}(1-v-vB_I\eta)K_{IC}^2 & (plane\ stress) \end{cases} \quad (16)$$

where B_I is the biaxiality ratio for the pure mode I loading. Part of the derivation process can refer to Hua [46]. When different fracture parameters (i.e., K_I, K_{II}, K_{III} and T) are confirmed, the in-plane and out-of-plane fracture angles can be obtained by Equations (13) and (14), and the mixed-mode fracture toughness ratio can also be predicted by Equations (12) and (16).

Figure 15 shows the relationship between mixed-mode I/II and I/III fracture toughness ratios under the plane stress condition. It can be seen that the GMTSED criterion had a high sensitivity in predicting I/II mixed fractures. The ratio of pure mode II fracture toughness change under different positive and negative T-stresses was more than 220%. However, the prediction of a mixed-mode I/III fracture using GMTSED criterion was very poor. As shown in Figure 16, the predicted value of the GMTSED criterion under the plane strain condition with different T-tress had a good sensitivity to I/II and I/III mixed-mode fracture toughness when ν = 0.35, where the value of pure III mode fracture toughness decreased regardless of the positive and negative T-stresses. Therefore, T-stress cannot be ignored in investigations of mixed-mode fractures. In mixed-mode fracture experiments, the mixed-mode fracture toughness is reduced under the influence of positive T-stress, which makes the material more vulnerable to failure.

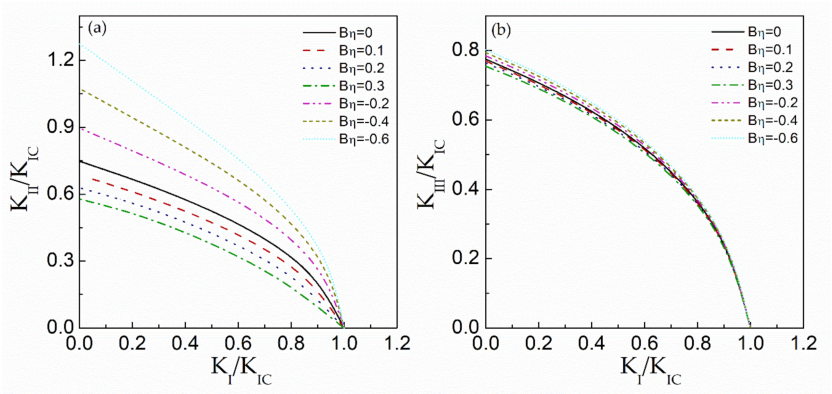


Figure 15. Mixed fracture toughness–predicted values of the fracture criterion under plane stress. (**a**) The mixed mode I/II fracture toughness–predicted values. (**b**) The mixed mode I/III fracture toughness–predicted values.

When comparing and analyzing the experimental data with the GMTSED criterion and other criteria, it was found that the predicted value calculated by the GMTSED criterion was in good agreement with the experimental data, whether for a mixed-mode I/II fracture or I/III fracture, as shown in Figure 17. Wang [55] also believed that the crack propagation and failure of material cannot be effectively judged only on the stress or strain of a certain point at the crack tip in reaching the maximum value, and that energy is more appropriate. Moreover, the prediction of mixed-mode I/II/III fractures was also consistent. As shown in Figure 18, under any mixed-mode I/II/III fracture model, the experimental data of effective SIF K_{eff} and the predicted value of GMTSED criterion agreed well over a large range. There was a slight deviation when the experimental data was very small. That can be considered to play the role of a safety factor in engineering protection when the prediction results are larger than the experimental data. In general, the predicted values of the GMTSED criterion were in good agreement with the experimental values. The GMTSED criterion was applicable to the three-dimensional mixed-mode I/II/III fracture.

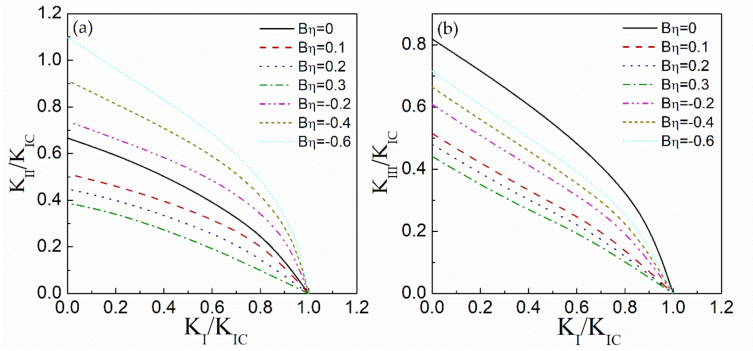


Figure 16. Mixed fracture toughness–predicted values of the fracture criterion under plane strain with $\nu = 0.35$. (**a**) The mixed mode I/II fracture toughness–predicted values. (**b**) The mixed mode I/III fracture toughness–predicted values.

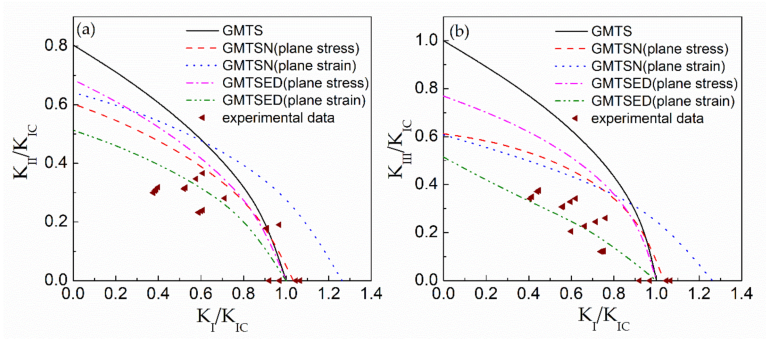


Figure 17. Mixed fracture toughness–predicted values of the fracture criterion and the testing data for sandstone. (**a**) The mixed mode I/II fracture toughness–predicted values. (**b**) The mixed mode I/III fracture toughness–predicted values.

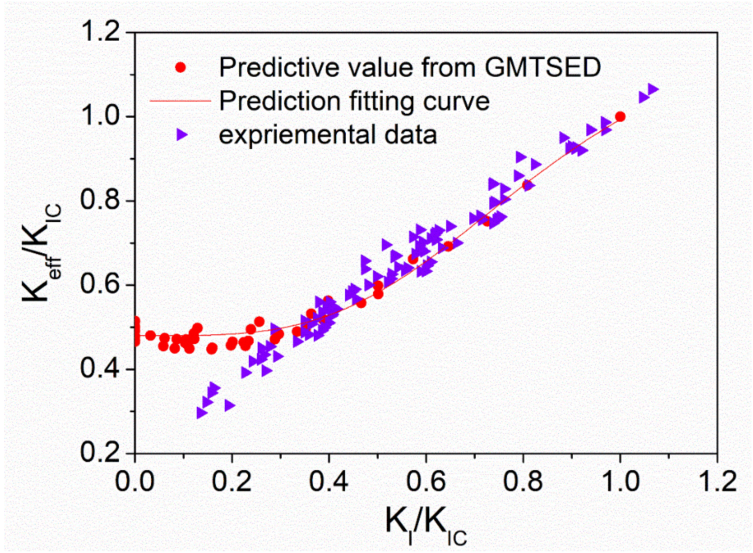


Figure 18. Effective SIF predicted values of the fracture criterion and the testing data for sandstone.

4. Conclusions

In this study, a TPB-IC specimen of arbitrary crack forms was proposed. Through various finite element analyses of the TPB-IC specimens, the fracture parameters, SIFs and T-stresses, including biaxiality ratio B, were obtained at different crack height ratios a/W and horizontal and vertical crack deflection angles α and β. The TPB-IC specimen could

achieve mixed-mode I/II/III fractures through the analysis of SIFs compared with the traditional three-point bending specimen. When the horizontal deflection angle α changed, the mixed-mode I/III fracture was affected. The value of horizontal deflection angle β affected the mixed-mode I/II fracture. It was shown that the T-stress played an important role in mixed-mode fractures through analysis of the biaxiality ratio B.

The mixed-mode fracture experiments for TPB-IC specimens were carried out using sandstone, and the corresponding mixed-fracture toughness was obtained. The GMTSED criterion considering T-stress was proposed and used to analyze the experimental results. The GMTSED criterion proved once again that T-stress cannot be ignored in the prediction of mixed-mode fracture toughness. Compared with the GMTS and GMTSN criteria, it was found that the three-dimensional GMTSED criterion under plane strain considering T-stress could successfully predict the mixed-mode fracture toughness.

Author Contributions: Conceptualization, X.P.; methodology, X.P.; validation, X.P., J.H., Z.G., W.H. and S.D.; formal analysis, X.P.; investigation, X.P.; resources, X.P., J.H. and Z.G.; data curation, X.P. and W.H.; writing—original draft preparation, X.P.; writing—review and editing, S.D.; visualization, X.P.; supervision, W.H. and S.D.; project administration, X.P.; funding acquisition, W.H. and S.D. All authors have read and agreed to the published version of the manuscript.

Funding: This work was funded by the National Natural Science Foundation of China (No. 11872042), the Sichuan Science and Technology Program (Nos. 2018JY0024 and 2019YJ0156), the China Postdoctoral Science Foundation (2019M653395) and the Postdoctoral Research Foundation of Sichuan University (2019SCU12049).

Institutional Review Board Statement: Not applicable.

Informed Consent Statement: Not applicable.

Data Availability Statement: The data presented in this study are available in Appendix A.

Conflicts of Interest: The authors declare no conflict of interest.

Appendix A

Table A1. The geometric parameters of specimens and fracture loads obtained for the tested sandstone material under different loading modes.

α (°)	β (°)	W (mm)	B (mm)	P (N)	P_{ave} (N)	β (°)	W (mm)	B (mm)	P (N)	P_{ave} (N)
0	0	40.0	20.0	268.324	255.631	15	39.0	20.0	275.573	268.925
		39.8	20.0	246.565			39.0	20.0	275.573	
		39.0	20.0	227.227			39.0	19.8	256.234	
	30	40.7	20.0	280.407	263.486	45	40.0	20.0	268.321	402.481
		39.0	20.0	297.328			38.5	20.0	432.697	
		40.0	19.3	246.565			39.0	20.0	377.099	
		39.0	20.0	251.400			39.0	20.0	418.193	
		39.4	20.0	258.651			39.0	20.0	381.934	
	60	39.8	20.0	565.649	530.598					
		39.0	20.0	536.641						
		39.0	20.0	529.389						
		39.0	19.0	490.713						

Table A1. *Cont.*

α (°)	β (°)	W (mm)	B (mm)	P (N)	P_{ave} (N)	β (°)	W (mm)	B (mm)	P (N)	P_{ave} (N)
15	0	39.3	19.5	193.384	192.176	15	40.6	20.0	258.651	267.716
		40.0	19.2	193.384			39.0	19.6	263.486	
		39.5	19.5	190.967			39.6	19.4	268.321	
		39.4	19.3	190.967			39.4	19.6	280.407	
	30	39.0	20.0	336.005	315.458	45	38.8	20.0	396.438	428.467
		40.0	20.0	290.076			40.2	20.0	468.957	
		39.0	19.8	304.580			39.0	20.0	442.366	
		39.0	19.0	331.171			39.0	19.8	406.107	
	60	39.0	20.0	580.153	601.909					
		39.5	20.0	594.657						
		39.0	20.0	597.074						
		39.5	19.2	635.751						
30	0	40.0	20.0	244.148	213.327	15	39.2	20.0	265.903	291.285
		38.0	19.8	210.305			40.5	20.0	277.99	
		40.0	20.0	212.723			40.2	20.0	306.998	
		39.8	19.5	186.132			39.0	20.0	314.249	
	30	40.6	20.0	398.855	390.999	45	39.0	20.0	418.193	471.374
		40.5	20.0	396.438			39.0	20.0	497.964	
		41.0	20.0	435.115			41.5	20.0	510.051	
		39.0	20.2	333.588			39.0	19.7	459.288	
	60	39.2	20.0	669.593	607.347					
		39.7	20.0	568.066						
		40.0	20.0	601.908						
		39.8	19.0	589.822						
45	0	39.0	20.0	253.817	253.213	15	39.0	20.0	297.328	299.141
		41.0	19.3	246.565			40.0	20.0	294.911	
		39.4	20.0	268.321			38.0	20.0	287.659	
		39.8	19.8	244.148			40.0	20.2	316.667	
	30	40.5	20.0	328.753	371.056	45	40.5	20.0	478.626	484.065
		40.0	20.0	352.926			40.6	20.0	456.870	
		40.9	20.0	394.020			39.0	20.0	442.366	
		39.0	20.4	408.524			40.0	19.8	558.397	
	60	40.5	20.0	613.995	569.879					
		41.0	20.0	464.122						
		40.0	19.3	597.074						
		39.3	19.2	604.326						
60	0	41.0	20.0	336.005	340.235	15	40.6	20.0	369.847	377.706
		39.0	20.0	338.422			39.5	20.0	311.832	
		41.0	20.0	343.257			38.8	19.5	391.603	
		39.0	20.0	343.257			39.3	19.6	437.532	
	30	39.5	20.0	323.919	384.351	45	40.0	20.0	495.547	514.886
		39.4	20.0	350.509			40.2	20.0	536.641	
		39.5	20.0	420.611			40.0	20.0	464.122	
		40.0	19.0	442.366			40.0	19.2	563.232	
	60	39.0	20.0	616.412	585.592					
		40.0	20.0	551.145						
		38.4	20.0	563.232						
		39.0	19.2	611.578						

Table A2. The SIFs and T-stresses of experimental fracture results obtained for the tested sandstone material under different loading modes.

α (°)	β (°)	$K_{Iave}(Mpa\sqrt{m})$	$K_{IIave}(Mpa\sqrt{m})$	$K_{IIIave}(Mpa\sqrt{m})$	T_{ave}(Mpa)
0	0	0.380	0.000	0.000	0.116
	15	0.356	0.070	0.000	0.370
	30	0.238	0.094	0.000	0.710
	45	0.212	0.128	0.000	1.290
	60	0.147	0.117	0.000	1.585
15	0	0.283	0.000	0.047	0.119
	15	0.336	0.068	0.053	0.395
	30	0.273	0.112	0.038	0.863
	45	0.213	0.126	0.050	1.289
	60	0.159	0.125	0.047	1.696
30	0	0.260	0.000	0.089	0.186
	15	0.302	0.068	0.099	0.466
	30	0.277	0.102	0.112	0.864
	45	0.202	0.114	0.099	1.188
	60	0.137	0.104	0.084	1.421
45	0	0.221	0.000	0.122	0.231
	15	0.233	0.041	0.134	0.383
	30	0.197	0.070	0.129	0.636
	45	0.154	0.085	0.123	0.882
	60	0.095	0.073	0.098	0.960
60	0	0.162	0.000	0.137	0.254
	15	0.167	0.032	0.147	0.185
	30	0.122	0.047	0.124	0.332
	45	0.097	0.059	0.123	0.490
	60	0.057	0.052	0.099	0.540

Table A3. The coefficients of Equation (12) under the plane stress state.

$$\begin{cases} m_{11} = cos^2\phi cos^4\frac{\theta}{2}\left[(1+v)cos^2\phi cos^2\frac{\theta}{2} - 2v\right] \\ m_{22} = 3cos^2\phi cos^2\frac{\theta}{2}sin^2\frac{\theta}{2}\left[3(1+v)cos^2\phi cos^2\frac{\theta}{2} - 2v\right] \\ m_{33} = (1+v)cos^2\frac{\theta}{2}sin^2 2\phi \\ m_{44} = cos^2\phi sin^2\theta\left[(1+v)cos^2\phi sin^2\theta - v\right] \\ m_{12} = 2cos^2\phi cos^3\frac{\theta}{2}sin\frac{\theta}{2}\left[4v - 3(1+v)cos^2\phi cos^2\frac{\theta}{2}\right] \\ m_{13} = -2cos^2\frac{\theta}{2}sin2\phi\left[(1+v)cos^2\phi cos^2\frac{\theta}{2} - v\right] \\ m_{23} = cos\phi sin\theta\left[3(1+v)cos^2\phi cos^2\frac{\theta}{2} - v\right] \\ m_{14} = -cos\frac{\theta}{2}cos^2\phi\left[2vsin^2\theta + \frac{v(cos\theta-1)}{2} - (1+v)cos^2\phi sin^2\theta(cos\theta+1)\right] \\ m_{24} = cos^2\phi cos^2\frac{\theta}{2}sin\frac{\theta}{2}\left[3v + 8vsin^2\frac{\theta}{2} - 24(1+v)sin^2\theta cos^2\phi\right] \\ m_{34} = -cos\frac{\theta}{2}sin2\phi\left[2(1+v)sin^2\theta cos^2\phi - v\right] \end{cases}$$

Table A4. The coefficients of Equation (12) under the plane strain state.

$$
\begin{cases}
m_{11} = (1+v)\cos^2\frac{\theta}{2}\left[\cos^4\frac{\theta}{2}\cos^4\phi + v\sin^2 2\phi\cos^2\frac{\theta}{2} - 2v\cos\frac{\theta}{2}\cos^2\phi - v^2\sin^2 2\phi\right] \\
m_{22} = (1+v)\cos^2\phi\sin^2\frac{\theta}{2}\left[-4v^2\sin^2 2\phi - 6v\cos 2\phi\cos^2\frac{\theta}{2} + 9\cos^4\frac{\theta}{2}\cos^2\phi\right] \\
m_{33} = (1+v)\cos^2\frac{\theta}{2}\sin^2 2\phi \\
m_{44} = \left(\cos^2\phi\sin^2\theta + \sin^2\phi\right)\left[(1+v)\left(\cos^2\phi\sin^2\theta + \sin^2\phi\right) - 2v\right] \\
m_{12} = (1+v)\sin\theta\left[v^2\sin^2 2\phi + 2v\cos 2\phi\cos^2\frac{\theta}{2}(\cos 2\phi - 1) - 3\cos^4\frac{\theta}{2}\cos^4\phi\right] \\
m_{13} = 2(1+v)\cos^2\frac{\theta}{2}\sin 2\phi\left(v\cos 2\phi - \cos^2\frac{\theta}{2}\cos^2\phi\right) \\
m_{23} = (1+v)\sin\theta\sin 2\phi\left[-v + 2v\sin^2\phi + 3\cos^2\frac{\theta}{2}\cos^2\phi\right] \\
m_{14} = 2(1+v)\cos\frac{\theta}{2}\cos^2\phi\sin^2\phi\left(2v\sin^2\phi + \cos^2\frac{\theta}{2}\cos^2\phi - v\right) + 2v\cos\frac{\theta}{2}\sin^2\phi\left[2(1+v)\sin^2\phi - 3v - 1\right] + 2\cos^3\frac{\theta}{2}\cos^2\phi\left[(1+v)\sin^2\phi - v\right] \\
m_{24} = 2\sin\frac{\theta}{2}\sin^2\phi\left[v(1+3v) + 2(1+v)\sin^2\phi + 3\cos\frac{\theta}{2}\cos^2\phi\right] + \sin\frac{\theta}{2}\cos^2\phi\cos^2\frac{\theta}{2}\left[8v(1+v)\sin^2\frac{\theta}{2} + 8v\sin^2\frac{\theta}{2}\sin^2\phi + 3\sin^2\theta\cos^2\phi + 6v\right] \\
m_{34} = 2\cos\frac{\theta}{2}\sin 2\phi\left[v + (1+v)\left(\cos^2\phi\sin^2\theta + \sin^2\phi\right)\right]
\end{cases}
$$

References

1. Columbus, D.; Grujicic, M. A comparison of mode I fracture behavior of fcc and bcc metallic materials: A discrete dislocation analysis. *Appl. Surf. Sci.* **2001**, *180*, 138–161. [CrossRef]
2. Horovistiz, A.L.; De Campos, K.A.; Shibata, S.; Prado, C.C.; Hein, L.R.D.O. Fractal characterization of brittle fracture in ceramics under mode I stress loading. *Mater. Sci. Eng. A* **2010**, *527*, 4847–4850. [CrossRef]
3. Ayatollahi, M.; Moghaddam, M.R.; Razavi, S.; Berto, F. Geometry effects on fracture trajectory of PMMA samples under pure mode-I loading. *Eng. Fract. Mech.* **2016**, *163*, 449–461. [CrossRef]
4. Bura, E.; Seweryn, A. Mode I fracture in PMMA specimens with notches—Experimental and numerical studies. *Theor. Appl. Fract. Mech.* **2018**, *97*, 140–155. [CrossRef]
5. Iqbal, M.; Mohanty, B. Experimental calibration of stress intensity factors of the ISRM suggested cracked chevron-notched Brazilian disc specimen used for determination of mode-I fracture toughness. *Int. J. Rock Mech. Min. Sci.* **2006**, *43*, 1270–1276. [CrossRef]
6. Iqbal, M.J.; Mohanty, B. Experimental Calibration of ISRM Suggested Fracture Toughness Measurement Techniques in Selected Brittle Rocks. *Rock Mech. Rock Eng.* **2006**, *40*, 453–475. [CrossRef]
7. Zuo, J.-P.; Xie, H.-P.; Dai, F.; Ju, Y. Three-point bending test investigation of the fracture behavior of siltstone after thermal treatment. *Int. J. Rock Mech. Min. Sci.* **2014**, *70*, 133–143. [CrossRef]
8. Ameri, M.; Mansourian, A.; Pirmohammad, S.; Aliha, M.; Ayatollahi, M. Mixed mode fracture resistance of asphalt concrete mixtures. *Eng. Fract. Mech.* **2012**, *93*, 153–167. [CrossRef]
9. Razmi, A.; Mirsayar, M. On the mixed mode I/II fracture properties of jute fiber-reinforced concrete. *Constr. Build. Mater.* **2017**, *148*, 512–520. [CrossRef]
10. Ayatollahi, M.; Aliha, M. Wide range data for crack tip parameters in two disc-type specimens under mixed mode loading. *Comput. Mater. Sci.* **2007**, *38*, 660–670. [CrossRef]
11. Berto, F.; Lazzarin, P.; Gomez, F.J.; Elices, M. Fracture assessment of U-notches under mixed mode loading: Two procedures based on the 'equivalent local mode I' concept. *Int. J. Fract.* **2007**, *148*, 415–433. [CrossRef]
12. Gómez, F.J.; Elices, M.; Berto, F.; Lazzarin, P. Fracture of V-notched specimens under mixed mode (I + II) loading in brittle materials. *Int. J. Fract.* **2009**, *159*, 121–135. [CrossRef]
13. Dong, S. Theoretical analysis of the effects of relative crack length and loading angle on the experimental results for cracked Brazilian disk testing. *Eng. Fract. Mech.* **2008**, *75*, 2575–2581. [CrossRef]
14. Dong, S.; Wang, Y.; Xia, Y. Stress intensity factors for central cracked circular disk subjected to compression. *Eng. Fract. Mech.* **2004**, *71*, 1135–1148. [CrossRef]
15. Dong, S.; Wang, Y.; Xia, Y. A finite element analysis for using Brazilian disk in split Hopkinson pressure bar to investigate dynamic fracture behavior of brittle polymer materials. *Polym. Test.* **2006**, *25*, 943–952. [CrossRef]
16. Hua, W.; Dong, S.; Li, Y.; Wang, Q. Effect of cyclic wetting and drying on the pure mode II fracture toughness of sandstone. *Eng. Fract. Mech.* **2016**, *153*, 143–150. [CrossRef]
17. Hua, W.; Dong, S.; Peng, F.; Li, K.; Wang, Q. Experimental investigation on the effect of wetting-drying cycles on mixed mode fracture toughness of sandstone. *Int. J. Rock Mech. Min. Sci.* **2017**, *93*, 242–249. [CrossRef]
18. Hua, W.; Li, J.; Dong, S.; Pan, X. Experimental Study on Mixed Mode Fracture Behavior of Sandstone under Water–Rock Interactions. *Processes* **2019**, *7*, 70. [CrossRef]
19. Aliha, M.; Ayatollahi, M.; Smith, D.; Pavier, M. Geometry and size effects on fracture trajectory in a limestone rock under mixed mode loading. *Eng. Fract. Mech.* **2010**, *77*, 2200–2212. [CrossRef]
20. Aliha, M.R.M.; Ayatollahi, M.R. Brittle fracture evaluation of a fine grain cement mortar in combined tensile-shear deformation. *Fatigue Fract. Eng. Mater. Struct.* **2010**, *32*, 987–994. [CrossRef]
21. Pantano, A.; Averill, R.C. A penalty-based finite element interface technology. *Comput. Struct.* **2002**, *80*, 1725–1748. [CrossRef]
22. Pantano, A.; Averill, R.C. A penalty-based interface technology for coupling independently modeled 3D finite element meshes. *Finite Elem. Anal. Des.* **2007**, *43*, 271–286. [CrossRef]
23. Pantano, A. Cohesive Model for the Simulation of Crack Initiation and Propagation in Mixed-Mode I/II in Composite Materials. *Appl. Compos. Mater.* **2019**, *26*, 1207–1225. [CrossRef]
24. Margevicius, R.; Riedle, J.; Gumbsch, P. Fracture toughness of polycrystalline tungsten under mode I and mixed mode I/II loading. *Mater. Sci. Eng. A* **1999**, *270*, 197–209. [CrossRef]
25. Choi, S.; Zhu, D.; Miller, R. Fracture behavior under mixed-mode loading of ceramic plasma-sprayed thermal barrier coatings at ambient and elevated temperatures. *Eng. Fract. Mech.* **2005**, *72*, 2144–2158. [CrossRef]
26. Ayatollahi, M.; Aliha, M.; Hassani, M. Mixed mode brittle fracture in PMMA—An experimental study using SCB specimens. *Mater. Sci. Eng. A* **2006**, *417*, 348–356. [CrossRef]
27. Aliha, M.; Saghafi, H. The effects of thickness and Poisson's ratio on 3D mixed-mode fracture. *Eng. Fract. Mech.* **2013**, *98*, 15–28. [CrossRef]
28. Aliha, M.; Ayatollahi, M. Mixed mode I/II brittle fracture evaluation of marble using SCB specimen. *Procedia Eng.* **2011**, *10*, 311–318. [CrossRef]

29. Funatsu, T.; Kuruppu, M.; Matsui, K. Effects of temperature and confining pressure on mixed-mode (I–II) and mode II fracture toughness of Kimachi sandstone. *Int. J. Rock Mech. Min. Sci.* **2014**, *67*, 1–8. [CrossRef]
30. Ameri, B.; Taheri-Behrooz, F.; Aliha, M. Fracture loads prediction of the modified 3D-printed ABS specimens under mixed-mode I/II loading. *Eng. Fract. Mech.* **2020**, *235*, 107181. [CrossRef]
31. Aliha, M.R.M.; Hosseinpour, G.R.; Ayatollahi, M.R. Application of Cracked Triangular Specimen Subjected to Three-Point Bending for Investigating Fracture Behavior of Rock Materials. *Rock Mech. Rock Eng.* **2012**, *46*, 1023–1034. [CrossRef]
32. Mousavi, S.; Aliha, M.; Imani, D. On the use of edge cracked short bend beam specimen for PMMA fracture toughness testing under mixed-mode I/II. *Polym. Test.* **2020**, *81*, 106199. [CrossRef]
33. Avci, A.; Akdemir, A.; Arikan, H. Mixed-mode fracture behavior of glass fiber reinforced polymer concrete. *Cem. Concr. Res.* **2005**, *35*, 243–247. [CrossRef]
34. Seifi, R.; Omidvar, N. Fatigue crack growth under mixed mode I + III loading. *Mar. Struct.* **2013**, *34*, 1–15. [CrossRef]
35. Liu, S.; Chao, Y.J.; Zhu, X. Tensile-shear transition in mixed mode I/III fracture. *Int. J. Solids Struct.* **2004**, *41*, 6147–6172. [CrossRef]
36. Aliha, M.; Bahmani, A.; Akhondi, S. Numerical analysis of a new mixed mode I/III fracture test specimen. *Eng. Fract. Mech.* **2015**, *134*, 95–110. [CrossRef]
37. Aliha, M.R.M.; Bahmani, A. Rock Fracture Toughness Study under Mixed Mode I/III Loading. *Rock Mech. Rock Eng.* **2017**, *50*, 1739–1751. [CrossRef]
38. Aliha, M.; Bahmani, A.; Akhondi, S. Determination of mode III fracture toughness for different materials using a new designed test configuration. *Mater. Des.* **2015**, *86*, 863–871. [CrossRef]
39. Aliha, M.; Bahmani, A.; Akhondi, S. A novel test specimen for investigating the mixed mode I+III fracture toughness of hot mix asphalt composites—Experimental and theoretical study. *Int. J. Solids Struct.* **2016**, *90*, 167–177. [CrossRef]
40. Bahmani, A.; Aliha, M.; Berto, F. Investigation of fracture toughness for a polycrystalline graphite under combined tensile-tear deformation. *Theor. Appl. Fract. Mech.* **2017**, *90*, 53–64. [CrossRef]
41. Lin, B.; Mear, M.E.; Ravi-Chandar, K. Criterion for initiation of cracks under mixed-mode I + III loading. *Int. J. Fract.* **2010**, *165*, 175–188. [CrossRef]
42. Ahmadi-Moghadam, B.; Taheri, F. An effective means for evaluating mixed-mode I/III stress intensity factors using single-edge notch beam specimen. *J. Strain Anal. Eng. Des.* **2013**, *48*, 245–257. [CrossRef]
43. Erdogan, F.; Sih, G.C. On the Crack Extension in Plates under Plane Loading and Transverse Shear. *J. Fluids Eng.* **1963**, *85*, 519–525. [CrossRef]
44. Chang, K.J. On the maximum strain criterion—A new approach to the angled crack problem. *Eng. Fract. Mech.* **1981**, *14*, 107–124. [CrossRef]
45. Ayatollahi, M.R.; Saboori, B. Maximum tangential strain energy density criterion for general mixed mode I/II/III brittle fracture. *Int. J. Damage Mech.* **2014**, *24*, 263–278. [CrossRef]
46. Hua, W.; Huang, J.; Pan, X.; Li, J.; Dong, S. An extended maximum tangential strain energy density criterion considering T-stress for combined mode I–III brittle fracture. *Fatigue Fract. Eng. Mater. Struct.* **2020**, *44*, 169–181. [CrossRef]
47. Bažant, Z.P.; Estenssoro, L.F. Surface singularity and crack propagation. *Int. J. Solids Struct.* **1979**, *15*, 405–426. [CrossRef]
48. Bidadi, J.; Akbardoost, J.; Aliha, M.R.M. Thickness effect on the mode III fracture resistance and fracture path of rock using ENDB specimens. *Fatigue Fract. Eng. Mater. Struct.* **2020**, *43*, 277–291. [CrossRef]
49. Patel, J.; Ayyar, A.; Peralta, P. Kink band evolution in polymer matrix composites under bending: A digital image correlation study. *J. Reinf. Plast. Compos.* **2020**, *39*, 852–866. [CrossRef]
50. Zhang, H.; Fu, D.; Song, H.; Kang, Y.; Huang, G.; Qi, G.; Li, J. Damage and Fracture Investigation of Three-Point Bending Notched Sandstone Beams by DIC and AE Techniques. *Rock Mech. Rock Eng.* **2015**, *48*, 1297–1303. [CrossRef]
51. Hua, W.; Dong, S.; Fan, Y.; Pan, X.; Wang, Q. Investigation on the correlation of mode II fracture toughness of sandstone with tensile strength. *Eng. Fract. Mech.* **2017**, *184*, 249–258. [CrossRef]
52. Hua, W.; Dong, S.; Li, Y.; Xu, J.; Wang, Q. The influence of cyclic wetting and drying on the fracture toughness of sandstone. *Int. J. Rock Mech. Min. Sci.* **2015**, *78*, 331–335. [CrossRef]
53. Dehestani, A.; Hosseini, M.; Beydokhti, A.T. Effect of wetting—Drying cycles on mode I and mode II fracture toughness of sandstone in natural (pH = 7) and acidic (pH = 3) environments. *Theor. Appl. Fract. Mech.* **2020**, *107*, 102512. [CrossRef]
54. Williams, M.L. The Bending Stress Distribution at the Base of a Stationary Crack. *J. Appl. Mech.* **1961**, *28*, 78–82. [CrossRef]
55. Wang, B. Material Strength: A Rational Nonequilibrium Energy Model for Complex Loadings. *J. Appl. Mech.* **2021**, *88*, 1–23. [CrossRef]